Finite element analysis of shear-critical reinforced concrete walls

İlker Kazaz*

Department of Civil Engineering, Atatürk University, 25240 Erzurum, Turkey

Abstract. Advanced material models for concrete are not widely available in general purpose finite element codes. Parameters to define them complicate the implementation because they are case sensitive. In addition to this, their validity under severe shear condition has not been verified. In this article, simple engineering plasticity material models available in a commercial finite element code are used to demonstrate that complicated shear behavior can be calculated with reasonable accuracy. For this purpose dynamic response of a squat shear wall that had been tested on a shaking table as part of an experimental program conducted in Japan is analyzed. Both the finite element and material aspects of the modeling are examined. A corrective artifice for general engineering plasticity models to account for shear effects in concrete is developed. The results of modifications in modeling the concrete in compression are evaluated and compared with experimental response quantities.

Keywords: shear; compression softening; squat wall; plasticity; finite element method; ANSYS.

1. Introduction

Complexity of concrete response under various loading regimes (uniaxial, biaxial or multi-axial) has been manifested (Chen 1982). Due to highly nonlinear nature of concrete material including cracking, crushing, tension stiffening, compression softening and bond-slip, accuracy of modeling reinforced concrete structures and components is strongly dependent on the material models.

Advanced material models capable of capturing different modes of nonlinear concrete response have been proposed and verified against test data by numerous researchers (Ramaswamy *et al.* 1994). However, these models are usually not to be found in commercial codes. Numerous parameters to define these models increase the accuracy, but they complicate the solution because they are problem dependent. Additionally, sophisticated numerical algorithms are required to implement these models. Another shortcoming of existing commercial finite element codes is that the available material models used for concrete were originally developed for metallic materials within the framework of plasticity theory. The idealization in material behavior for elastic unloading may not be a suitable approach for modeling the cyclic behavior of concrete since concrete exhibits stiffness degradation under cyclic loading (Mirmiran *et al.* 2000).

Despite these limitations, commercial finite element codes are used extensively for research purposes. Padmarajaiah and Ramaswamy (2002) investigated the flexural behavior of 15 fully/partially prestressed high strength concrete beams containing steel fibers using three-dimensional nonlinear finite elemental

---

* Corresponding author, Ph.D., E-mail: ilkkazaz@gmail.com

analysis. Later, Thomas and Ramaswamy (2006) reported the details of the finite element analysis of eleven shear critical partially prestressed concrete T-beams having steel fibers over partial or full depth. The ANSYS models in these studies accounted for the nonlinear phenomenon, such as, bond-slip of longitudinal reinforcements, post-cracking tensile stiffness of the concrete, stress transfer across the cracked blocks of the concrete and load sustenance through the bridging of steel fibers at crack interface. Kwan and Billington (2001) used a commercial finite element code to investigate the effects of nonlinear material models and their associated parameters on the cyclic response of reinforced concrete structural members. A significant outcome of their research is that although the adopted material models are able to represent flexure dominated behavior well, they can only indicate when shear-dominated hysteretic behavior is likely. They stated that further improvements are required in modeling cyclic shear deterioration in concrete constitutive model to capture the shear dominated behavior.

This account indicates that analysis of reinforced concrete members under shear and torsional effects requires special treatment of concrete material properties and laws. Results of several prediction exercises revealed the inadequacy of customary analysis procedures for such elements (OECD/NEA/CSNI report 1996). Realistic models for response governed by shear are few and seem not to have gained excessive application in finite element practice (Vecchio and Collins 1986, Belarbi and Hsu 1995). Bali and Hwang (2007) proposed an analytical procedure to predict the strength and deformation characteristics of squat walls that are in double curvature. The analytical model enables decomposing the total lateral deformation into bending, shear and slip components. Shayanfar and Safiey (2008) proposed a new hypoelasticity constitutive relationship that utilizes the rotation of material axis through successive iterations. The capabilities of the proposed relationships were verified against experimental results of reinforced concrete walls. It was demonstrated that model can account for the pre-and post-peak regimes of the concrete material effectively.

The objective of this study is to ascertain the adequacy of familiar monotonic plastic material models in predicting the response of shear-critical members and discuss modifications for improved results. A commercial finite element code, ANSYS, is used for the analysis. The structure analyzed here is a shear wall specimen that was tested as a part of an experimental program carried out by NUPEC (Nuclear Power Engineering Corporation of Japan) in the early 1990s to study the seismic design and performance of shear walls in nuclear reactor buildings (OECD/NEA/CSNI report 1996). It was a single story flanged shear wall with $h_w/l_w = 0.67$. The specimen was heavily damaged in the experiment. It was observed that the wall response was dominated by shear effects and significant strength loss led to the failure of the specimen as a result of sliding shear that developed near the base of the web wall.

The geometric and material properties and the loading program of the NUPEC specimen are described next. A description of material models used in this study and aspects of finite element modeling issues follows. Static analyses under monotonically increasing lateral loads are carried out to identify the most appropriate material constants. Static analyses proved to be crucial for material identification and were important in providing insight for the behavior of the structure before attempting complicated nonlinear time history analyses. During the analysis phase different aspects solid finite element and material models are discussed. Finally, effectiveness of the plasticity models is verified by re-calculating the measured seismic response of the specimen.

2. The test structure

2.1 Specimen description

The Nuclear Power Engineering Corporation of Japan (NUPEC) conducted an extensive experimental investigation for the seismic safety of nuclear facilities in the early 1990s. For this purpose, two full-scale flanged shear walls (ISP shear walls) were subjected to a series of seismic excitations on a shaking table. Two specimens (U-1 and U-2) with the same design specification were prepared and tested by applying the same input signals in order to ascertain the reproducibility of the test. The measurements on specimen U-1 were used for the analyses in this article (OECD/NEA/CSNI report 1996).

Fig. 1 shows the dimensions of the test specimens. The web wall had a thickness of 75 mm, the flange wall length was 3000 mm, the clear height 2020 mm, and the shear span ratio 0.8. The flange walls were 100 mm thick and 2980 mm long. The amount of reinforcement in the web was 1.2%, consisting of D6 bars (deformed bar, nominal diameter 6.35 mm) at a spacing of 70 mm were used in the web wall both for the vertical and horizontal reinforcement. D6 bars at 175 mm spacing were used for the vertical reinforcement of the flange walls. As an exception, D6 bars at 70 mm spacing were used for the vertical reinforcement over a region at the intersections of the web wall and the flange walls.

Additional weights were fixed at the upper and lower surfaces of the top slab as shown in Fig. 1. The total additional mass was 92.9 t, and the total mass of the specimen including the top slab amounted to 122.0 t.

2.2 Seismic input motion

The objective of the vibration test program was to identify the dynamic response characteristics of the specimens ranging from their elastic state to ultimate by applying input table acceleration records at increasing amplitudes. The seismic tests were carried out by applying artificial earthquake motions that had flat acceleration controlled region over the frequencies ranging from 14 to 4 Hz corresponding to the initial frequency (13.2 Hz) and reduced response frequencies, in order to avoid
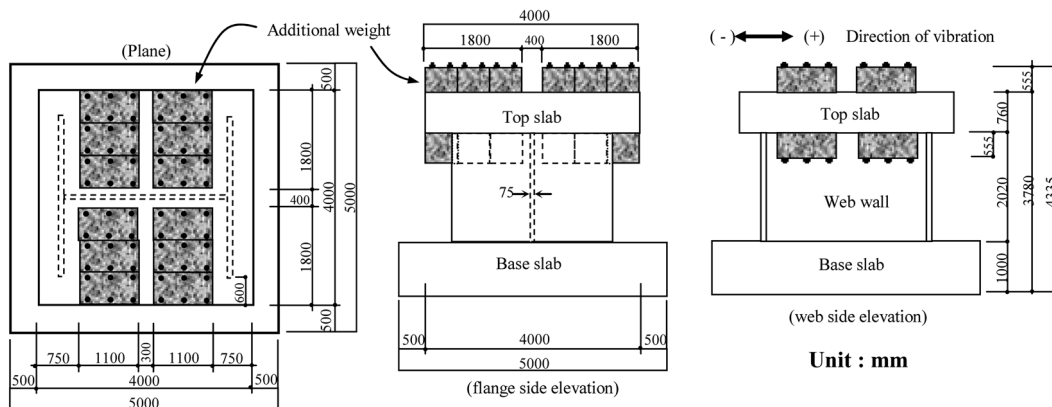

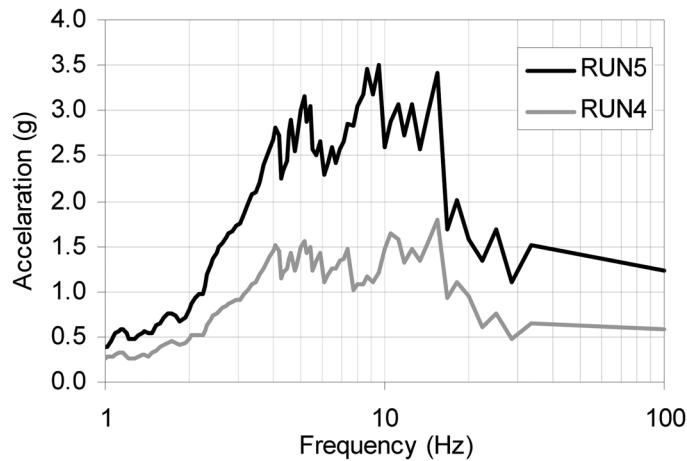Fig. 1 Dimensions of the specimen [adopted from NEA Committee Report (1996)]

Fig. 2 Five percent damped response spectrum of input acceleration for RUN-4 and -5

any response amplification induced by changes in the stiffness of the specimen. In the test, the specimens were excited in only one horizontal direction. The vibration test-runs were executed with five input acceleration levels. These runs were applied as RUN-1 to RUN-5 sequentially by increasing input acceleration levels of the same artificial wave. The 5 percent damped acceleration response spectra of the input motions RUN-4 and RUN-5 are given in Fig. 2. Their spectral similarity is noted.

For a more detailed description of the structure, material properties, loading program and measured response readers can refer to the NEA Committee project final report (OECD/NEA/CSNI report 1996).

2.3 Test results

The measured fundamental frequency of the specimen prior to the loading program was 13.2 Hz. After successive seismic excitations and the resulting continuous degradation of the stiffness, measured fundamental frequency reduced to approximately 7 Hz before final loading (RUN-5) when extensive damage in the structure occurred. Table 1 shows the change of natural frequency and the equivalent viscous damping ratio observed.

The state of cracks for the specimen after the final step (RUN-5) is visualized in Fig. 3. Initial shear cracks at the mid portion of the web wall were observed after RUN-2 and horizontal cracks of the flange walls were observed after RUN-4. Failure of the wall was a result of crushing of the concrete in the toe regions, which caused a plane of weakness leading to a sliding shear. The sliding

Table 1 Change of frequency and equivalent viscous damping ratio

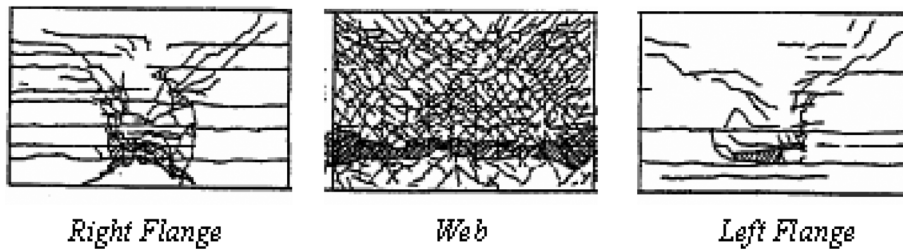| Test	Frequency (Hz)	Equivalent damping ratio (%)
Before RUN-1	13.2	1.1
Before RUN-3	11.3	2.5
Before RUN-4	9.9	3.0
Before RUN-5	7.7	4.0

Fig. 3 Visual observations of cracks and final web crushing failure of the wall (adopted from NEA Committee Report 1996)

of the wall was due to the punching action of the compressive strut through the flange walls, seen from the damage pattern in the flange wall as seen in Fig. 3. The sliding shear failure occurred 30 cm above the bottom of the web wall in RUN-5, which is a result of the confining effect of the very stiff base slab to the concrete near the base of the wall. Significant loss of strength and stiffness led to failure of the specimen.

3. Material models in ANSYS for concrete modeling

The ANSYS finite element program was our computational vehicle. The five-parameter Willam-Warnke (1975) criterion was used in combination with a solid element. The model assumes linear elastic stress-strain relationship until crushing. When used without a plasticity law it underestimates the deformation capacity of concrete because it neglects the nonlinearity in the ascending branch and the post-crushing strength of concrete in compression. ANSYS offers a number of rate independent kinematic and isotropic hardening plasticity options that can be used with the concrete element to model the compression behavior. The Drucker-Prager plasticity model (DP), von Mises bilinear (BISO) and multi-linear isotropic work hardening plasticity (MISO) are combined with the tensile failure criteria of Willam-Warnke material model (CONC). The notation given in parentheses refers to plasticity models defined here. These plasticity models, especially the Drucker-Prager model, require further discussion because parameters used to describe them differ for different loading conditions (stress states), since a combined yield surface is used.

In early finite element applications of concrete to model compression behavior, the von Mises plasticity (1928) model with isotropic hardening (BISO), kinematic hardening (BKIN) or combined hardening was used widely. Since this model is independent of the magnitude of the hydrostatic stresses, it may not be a suitable plasticity model for concrete in high compression (Chen 1982). The use of BISO material model is straightforward, because the model is directly calibrated with concrete strength in compression (f_c) and post elastic modulus (E_{cp}) of the bilinear curve. In the biaxial stress space or in plane stress condition ($\sigma_2 = 0$) von Mises yield surface is defined with an ellipse. At the risk of citing textbook information we indulge in a few reminders for completeness.

A smooth approximation to the Mohr-Coulomb surface was proposed by Drucker and Prager (1952) as a simple modification of the von Mises yield criterion in the form

$$f(I_1, J_2) = \alpha I_1 + \sqrt{J_2} - \tau_0 = 0 \qquad (1)$$

where α and τ_0 are positive material parameters. Under plane stress condition ($\sigma_2 = 0$), the invariants of

Table 2 Principal stresses, stress invariants, and Haigh-Westergaard coordinates at failure

Stress state	σ_1	σ_3	I_1	J_2	ξ	r	θ, degr.
Uniaxial tension	f_t	0	f_t	$f_t^2/3$	$f_t/\sqrt{3}$	$f_t\sqrt{2/3}$	0
Uniaxial compression	0	$-f_c$	$-f_c$	$f_c^2/3$	$-f_c/\sqrt{3}$	$f_c/\sqrt{2/3}$	60
Equi-biaxial compression	$-f_{bc}$	$-f_{bc}$	$-2f_{bc}$	$f_{bc}^2/3$	$-2f_{bc}/\sqrt{3}$	$f_{bc}\sqrt{2/3}$	0

the stress tensor are $I_1 = \sigma_1 + \sigma_3$ and $J_2 = (\sigma_1^2 + \sigma_3^2 - \sigma_1\sigma_3)/3$.

The input parameters α and τ_0 are interpreted in terms of c and ϕ of the Mohr-Coulomb (MC) model. The parameter c is the cohesion and ϕ is the angle of internal friction. The DP constants can be related to MC constants c and ϕ in several ways. In the case of three dimensional matching, if it is decided to have the two failure surfaces meet on the compressive meridian, the two sets of material constants are related by

$$\alpha = \frac{2\sin\phi}{\sqrt{3}(3-\sin\phi)} \qquad \tau_0 = \frac{6c\,\cos\phi}{\sqrt{3}(3-\sin\phi)} \tag{2}$$

If the tensile meridian is used

$$\alpha = \frac{2\sin\phi}{\sqrt{3}(3+\sin\phi)} \qquad \tau_0 = \frac{6c\,\cos\phi}{\sqrt{3}(3+\sin\phi)} \tag{3}$$

Variation in concrete response under various load regimes leads to different definitions of material constants at each. To relate the Drucker-Prager constants α and τ_0 to the Mohr-Coulomb constants c and ϕ in the biaxial stress space, two data points from material tests are required. Considering the uniaxial compression (f_c) and tension (f_t) tests and biaxial compression (f_{bc}) test conditions, the values of principal stresses, invariants I_1 and J_2, and Haigh-Westergaard coordinates ξ, r and θ are listed in Table 2. Here r is the deviatoric and ξ is the hydrostatic components of stress tensor and θ is called the Lode angle or the angle of similarity.

In the case of Drucker-Prager criterion, substituting the values at peak stress under uniaxial compression (f_c) and tension (f_t) and solving for the model parameters in Eq. (1), it is found

$$\alpha = \frac{f_c - f_t}{\sqrt{3}(f_c + f_t)} \tag{4}$$

$$\tau_0 = \frac{2f_c f_t}{\sqrt{3}(f_c + f_t)} \tag{5}$$

Under the plane stress condition, this criterion takes the form

$$4(\sigma_1^2 + \sigma_3^2) + \left(2 - 3\frac{f_c^2 + f_t^2}{f_c f_t}\right)\sigma_1\sigma_3 + 4(f_c - f_t)(\sigma_1 + \sigma_3) - 4f_c f_t = 0 \tag{6}$$

Depending on the ratio f_t/f_c, Eq. (6) becomes an ellipse, a parabola or a hyperbola. By matching the uniaxial strengths in tension and in compression, we obtain a reasonable approximation of the actual failure envelope in the quadrants that correspond to biaxial tension and to tension-compression. A good approximation in the biaxial compression range can be obtained by matching the uniaxial and equi-biaxial compressive (f_{bc}) strengths (Jirasek and Bazant 2001)

$$\alpha = \frac{f_{bc} - f_c}{\sqrt{3}(2f_{bc} - f_c)} \tag{7}$$

$$\tau_0 = \frac{f_{bc}f_c}{\sqrt{3}(2f_{bc} - f_c)} \tag{8}$$

Similar to Eq. (6), the criterion can be expressed in the form as given below to give a better approximation in the compressive region in plane stress conditions

$$\left(2 - 3\frac{f_{bc}}{f_c}\right)(\sigma_1^2 + \sigma_3^2) + \left(3\frac{(2f_{bc}^2 + f_c^2)}{f_c f_{bc}} - 8\right)\sigma_1\sigma_3 - 2(f_{bc} - f_c)(\sigma_1 + \sigma_3) + f_c f_{bc} = 0 \tag{9}$$

The different failure surfaces described above are plotted in normalized form in Fig. 4, in order to judge how well they approximate the concrete response in biaxial stress state. The Drucker-Prager yield surfaces defined with Eqs. (6) and (9) and von Mises yield criterion are plotted and compared with the biaxial test data of Kupfer *et al.* (1969). The research by Kupfer (1969) indicated that equi-biaxial compressive strength of concrete is 1.16 times larger than its uniaxial compressive strength (f_{bc}=1.16f_c). Similar experiments by Yin *et al.* (1987) resulted in a ratio of 1.3 for equi-biaxial to uniaxial compressive strength of concrete (f_{bc} = 1.3f_c). A default value of 1.2 for the failure surface in compression for the Willam-Warnke model compares better with the biaxial test results of Kupfer *et al.* (1969).

All models mimic with varying success the test data in the compressive quadrant. However, von Mises and Drucker-Prager plasticity models overestimate the strength in the remaining three quadrants. Fig. 4 can be considered as 3-D failure surface for states of stress that are biaxial or nearly biaxial. If the largest nonzero principal stresses are in the σ_1 and σ_3 directions, the yield or failure surfaces presented here will become slightly enlarged for σ_2 slightly smaller than zero (compressive) and will shrink inside for σ_2 slightly greater than zero (tensile).

When plasticity based models are combined with the Willam-Warnke concrete material option
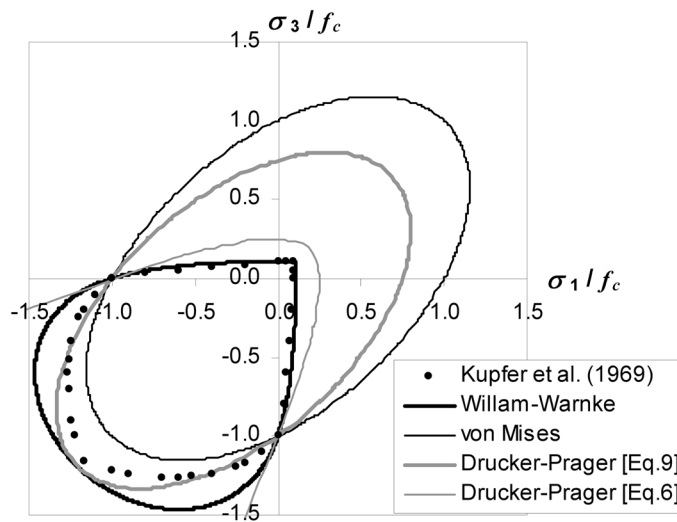

Fig. 4 Failure and yield surfaces for different material models

(CONC), the plasticity check is done before the cracking and crushing checks. Yielding or cracking of any material point within the model is evaluated on the basis of principal stresses. In view of this and simplification of the problem to a plane stress condition, it is obvious from Fig. 4 that in the quadrants for tension-tension and tension-compression the Willam-Warnke model will prevail until the cracking of concrete. Upon cracking a plane of weakness will form orthogonal to the crack direction which reduces the principal stress in this direction to zero as the solution converges. Following the stress relaxation due to cracking in the quadrant tension-compression both models will interact. In the quadrant for compression-compression pure plastic behavior will apply. This explanation leads to the following conclusion. Considering the cracked concrete with zero tensile stress in the direction perpendicular to crack face, the equivalent stress, which is used to determine whether plastic yielding occurs, depends only on the compressive strength of concrete for $\sigma_2 = 0$. While selecting the material parameters for Drucker-Prager material model to be used in combination with Willam-Warnke concrete model for the biaxial stress state, it must be ensured that these parameters result in close estimation of the actual compressive strength of concrete (f_c). This is to say that when either a tension-compression or compression-compression stress state exists it is more correct to model the concrete plasticity with equi-biaxial yield surface defined by Eq. (9) because this equation is valid in the compressive regime as well. The surface defined by Eq. (9) approximates the von Mises yield surface.

4. Finite element modeling and analyses

Finite element models of the specimens were created by using a solid reinforced concrete element (SOLID65) that is capable of modeling cracking in tension and crushing in compression following the material model after Willam-Warnke (1975). The element allows smeared reinforcement modeling as well.

Taking advantage of symmetry, a model representing half of the specimen was created and the corresponding boundary conditions were applied as in Fig. 5. The LINK8 element was used to
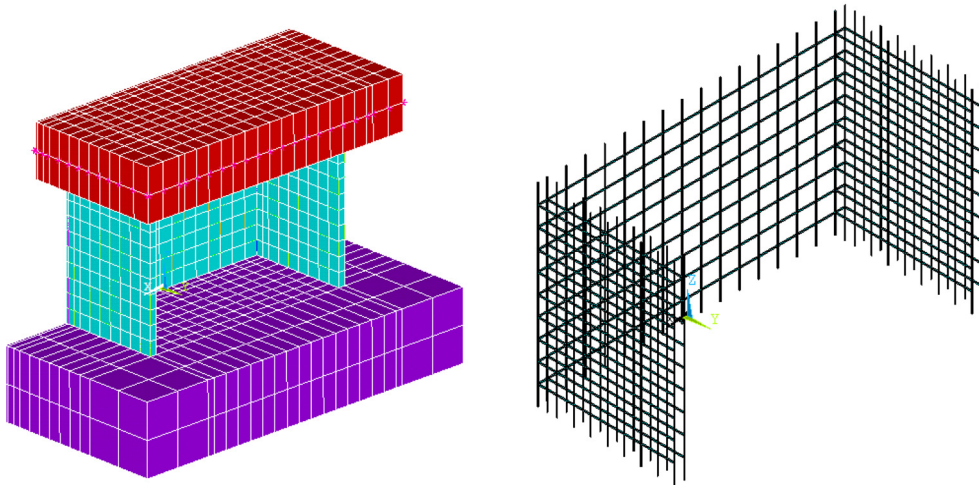

Fig. 5 Finite element model and the reinforcement grid of NUPEC wall

model the reinforcement. Concrete elements with $200 \times 200 \times 37.5$ mm dimension were used in the web wall. The actual reinforcement mesh in the wall had a grid spacing of 70×70 mm. In the interest of producing coincident nodes for concrete and rebar elements due to mesh size, the original reinforcement mesh at 70 mm spacing at vertical and horizontal was replaced by a grid where the bars are configured at 200 mm spacing. The rebar areas were adjusted to keep the total percentage of reinforcement unchanged at 1.2 percent. The additional masses are modeled with point mass elements assigned to mid section nodes of the top slab.

4.1 Calculation of the material parameters

Bilinear isotropic work hardening plasticity (BISO) is utilized for the material model of the steel reinforcement. The modulus of elasticity and yield strength used for steel are 184,400 MPa and 384 MPa, respectively. In the analyses the strain hardening of the steel is attributed a value of 1% ($E_{sp} = 0.01E_s$) to achieve better convergence.

The concrete material properties were provided by NUPEC (OECD/NEA/CSNI report 1996). The experimental concrete stress-strain curve was used to determine the constants of the material models mentioned above. The uni-axial compressive strength of the concrete (f_c) was taken as 28.6 MPa, the mean value of the concrete cylinder tests, and the tensile strength as 2.4 MPa. The initial modulus of elasticity and the Poisson's ratio were 22,900 MPa and 0.2, respectively. The von Mises plasticity models depend on elasto-plastic representation of the material behavior curve, so the nonlinear stress-strain curve of the concrete in uniaxial compression was bilinearized as in Fig. 6. The limiting compressive stress f_c'' is taken to be the average compressive stress equal to $0.85f_c$ corresponding to 23.8 MPa (Swamy and Qureshi 1974). Due to bilinearization the concrete modulus of elasticity reduces to 20,700 MPa. Using this value the first mode frequency of the model was calculated as 12.9 Hz, which is very close to measured fundamental frequency of the specimen given in Table 1. After model generation, modal analysis becomes crucial to verify the correctness of the finite element model.

For the case of Drucker-Prager model, inserting $f_c = 23.8$ MPa and $f_{bc} = 1.2f_c$ into Eqs. (7) and (8), parameters of Drucker-Prager yield surface are calculated as $\alpha = 0.0825$ and $\tau_0 = 11.78$ MPa, respectively. The yield surface has the same pattern as plotted in Fig. 4 utilizing Eq. (9). It is now required to
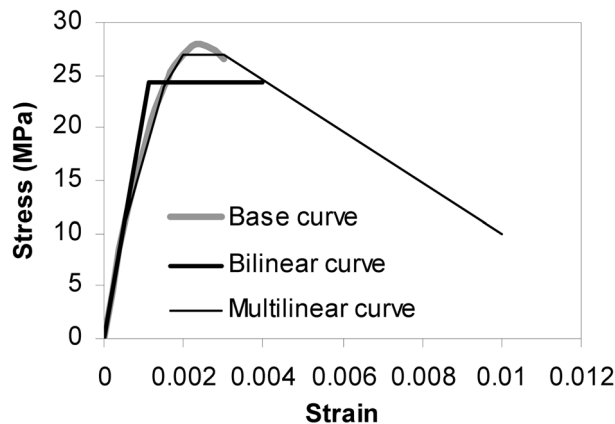

Fig. 6 Bilinearized and multilinear uniaxial stress-strain curves of concrete

express these parameters in terms of Mohr-Coulomb parameters, c and ϕ. Since Drucker-Prager model in ANSYS uses the outer cone approximation, with Eq. (2) these parameters are calculated as 9.72 MPa and 11.54º for the cohesion and the friction angle, respectively.

For multi-linear plasticity model (MISO), the material base curve was represented with five line segments as shown in Fig. 6. This is the only model that can be used to represent the strain-softening branch of concrete stress strain curve.

4.2 Finite element model calibration: Mesh size and element options

At the beginning it was emphasized that finite element analysis results are significantly affected by the adopted constitutive material laws. However, this statement is valid when the effects of numerical discretization are negligible. The properties of the model such as the mesh density and the element characteristics are also important aspects of the nonlinear finite element analysis procedure. The SOLID65 element has been vested with several features to increase the accuracy of the calculations and overcome restriction due to element behavior. However, these are case-dependent properties and must be calibrated for the application at hand.

The first FE analysis is seldom satisfactory. After trial runs differences between the calculations must be clarified. Since the displacement field within the element is calculated using linear interpolation functions and $2 \times 2 \times 2$ Gauss-quadrature integration scheme, it must be ensured that the mesh used is sufficiently fine to capture the behavior accurately. An extra model that is composed of concrete elements $70 \times 70 \times 37.5$ mm in size was created as shown in Fig. 7, and the reinforcing bars were discretized in their actual size and location to check the mesh size dependency of the results. The eight-node solid element exhibits shear locking, which is a defect associated with the linear element interpolation functions that contain no quadratic terms resulting in spurious shear strain. The element is too stiff to display the bending modes of displacement, if the finite element mesh is not fine enough. The "incompatible modes" formulation for modeling bending was invoked to avoid shear locking in the model.

The multilinear plasticity model with strain-softening as plotted in Fig. 6 was used in the calculations. The models were loaded by prescribed displacements at the mid section nodes of the top slab in all the analyses. The effect of gravity force is kept constant during the analyses.

The comparison of results of the three models is given in Fig. 8(a). It is seen that there is a considerable difference between the results of the fine and coarse mesh models in terms of both
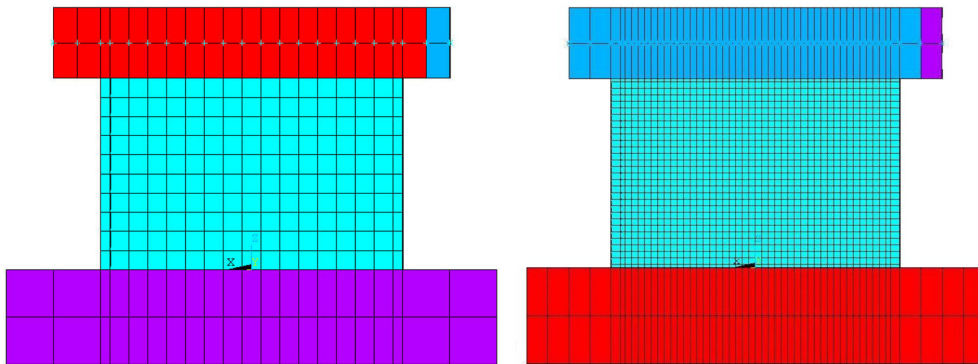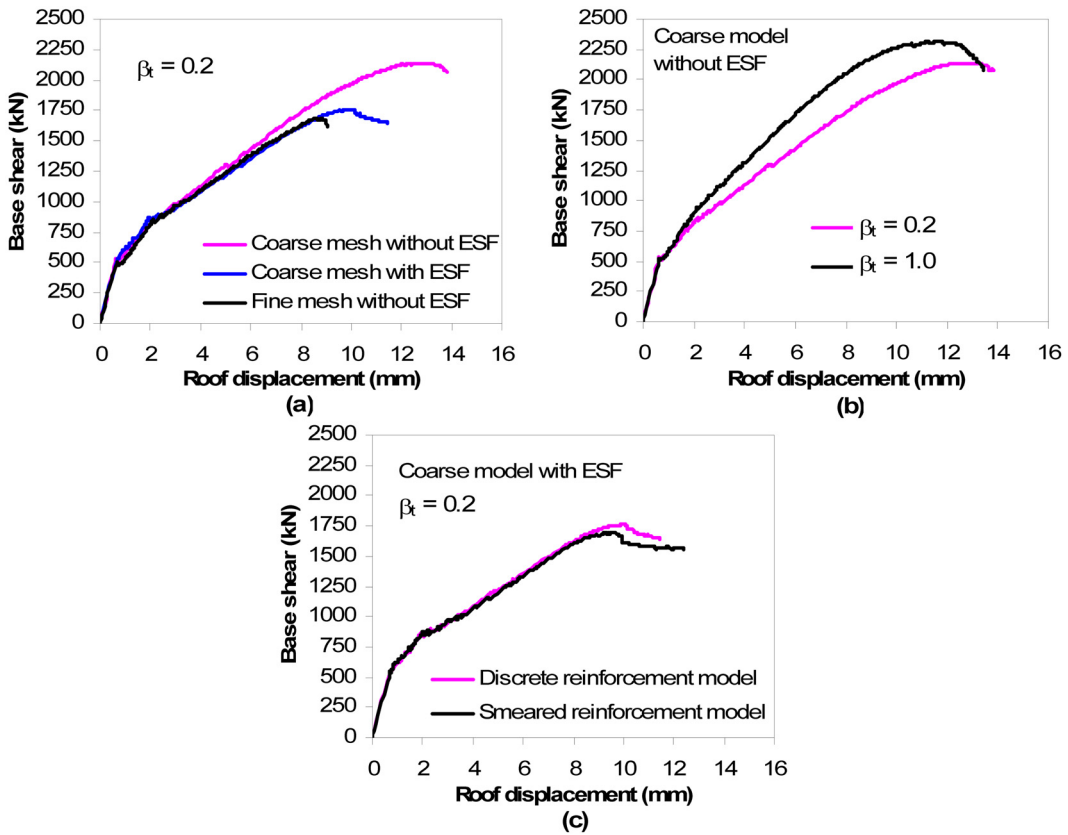

Fig. 7 Finite element meshes

Fig. 8 Numerical prediction of load-deflection response of the specimen indicating the influence of (a) mesh size, (b) shear transfer coefficient of concrete, and (c) reinforcement modeling

displacements and forces at the peak level. However, the coarse model utilizing extra element shapes is in good agreement with the fine mesh model curve, giving a slightly higher ultimate displacement limit to strength degradation. The reported values for experimentally observed drift ratio limits on squat walls at the peak load is in the range of 0.007~0.008 (Duffy *et al*. 1994). The calculated displacements are less than (0.005~0.007) the given limits. The initial stiffness of the models were found to be 837, 780 and 798 kN/mm for coarse mesh with no ESF, fine mesh with no ESF and coarse mesh with ESF, respectively. Since the three curves have approximately the same global stiffness until crushing strain is exceeded, the differences in the peak range point to a mesh size problem in local modeling.

When the softening property in the post-peak response is used in constitutive models, the finite element solutions are known to have spurious sensitivity to the mesh size and have difficulty in converging since low order elements such as the one used here is utilized in the finite element analysis (Maekawa *et al*. 2003, Červenka *et al*. 2005). The ISP wall had a large flexural capacity and adequate horizontal reinforcement to develop diagonal compression failure under monotonic loading. Plastic behavior in compression was observed to develop in the zone near the base of the wall. Analysis results indicated that the strains calculated in the compression region of fine mesh model are larger than the strains in coarse model at the same location. As the size of element in fine

mesh is nearly three times smaller than the element in coarse mesh, the strains are far more sensitive to nodal deformations from which they are calculated. Consequently, smaller elements can detect the softening earlier than larger ones. Since the global behavior is affected by local response in the compression zone of the web wall, mesh density in the localized damage region significantly affects the accuracy of the results.

These analyses also showed that numerical values assigned to shear transfer coefficients for open (β_t) and closed (β_c) cracks can play a significant role on the load-deflection response of the model. A shear transfer coefficient, β_t, is used to introduce a shear strength reduction factor for loading conditions which induce sliding shear across the crack face. Typical shear transfer coefficients range from 0.0 to 1.0, with 0.0 representing a smooth crack (complete loss of shear transfer) and 1.0 representing a rough crack (no loss of shear transfer). In line with previous studies (Hemmaty, 1998) values of 0.2 and 1.0 were adopted as shear transfer coefficients for open and closed cracks, respectively. The effect of shear transfer coefficient is obvious in Fig. 8(b).

When a concrete panel is reinforced by a dense reinforcing mesh and the change of internal forces from one bar to the next is small, the net effect may be considered as "smeared". For monotonic loading conditions this modeling technique was found to be effective, but for purposes of calculating rebar stresses accurately, discrete reinforcement modeling was preferred in model generation. In Fig. 8(c), the comparison of analytical prediction of load-deflection response of the specimen indicating the influence of reinforcement modeling as discrete and smeared form is given. It is seen from this figure that both modeling strategy yields equivalent responses for monotonically increasing loads.

It was decided that the mesh size of the coarse model in Fig. 5 and solid finite elements with extra element shapes formulation would be appropriate for further analysis purposes.

4.3 ISP Wall analysis

The force displacement response of the NUPEC wall was calculated by using the three plasticity models described above. The finite element model in Fig 5 was used. The Extra Shape Function
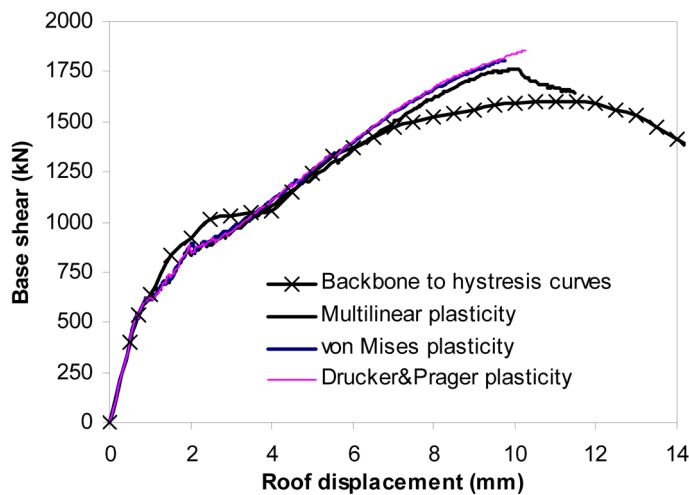

Fig. 9 Comparison of calculated load-deflection curves with the experimental dynamic back bone curve plotted against the hysteretic curves of the five experiments

feature of ANSYS was included in element interpolation functions. Shear transfer coefficients for open and closed cracks were taken as 0.2 and 1.0, respectively. A displacement controlled loading scheme was adopted. The displacement was applied on the mid-section node of the top slab. The calculated response curves are presented in Fig. 9. Given in this figure is also the load-displacement backbone curve plotted as an outer envelope to the five experimental hysteresis curves. For DP and VM models the calculations were stopped when net section yielding had occurred resulting in large displacements for small increments of load.

For all the material models, the ultimate displacement at the peak load of the specimen was calculated in the range of 10 mm, which is 16 percent smaller than the displacement value at the initiation of strength degradation in the experimental response curve. All curves are very similar. It is displayed in Fig. 9 that the calculated response curves slightly underestimate the actual response over a certain region after the cracking load is exceeded ($F_{cr} \approx 600$ kN). Tests on reinforced concrete elements (Vecchio and Collins 1993) have demonstrated that even after extensive cracking, tensile stresses may still exist in the cracked concrete and that these stresses significantly increase the ability of the cracked concrete to resist shear stresses. Since the cracking was handled by reducing the tensile stresses in the crack plane to zero, this led to this underestimation.

Comparison of the predicted and experimentally measured response revealed that beyond 6 mm roof drift the predicted response overestimates the measurement. This is within expectations since the response obtained from monotonically increasing static loading was compared with a response that is cyclic in nature, which causes stiffness and strength deterioration in concrete. In order to capture the experimentally measured response, it is required either to modify the finite element model or to calibrate the material model to incorporate the effects of load history and concrete mechanics.

At this point, the analytical response of the specimen will be investigated in detail. A snapshot of the principal strains from the analysis phase when the top slab displacement is approximately 5.5 mm is given in Fig. 10. The tensile strain developed at the lower left region of the web wall is around 0.004. The inclination of the principal compressive strains (ε_3) is approximately 45 degrees. Experiments conducted by Vecchio and Collins (1993) show that compressive strength of concrete subjected to biaxial tension-compression (situations likely to produce shear mechanisms) decreases. The principal compressive stress in concrete was found to be a function not only of the principal compressive strain but also of the co-existing principal tensile strain. More clearly, cracked concrete

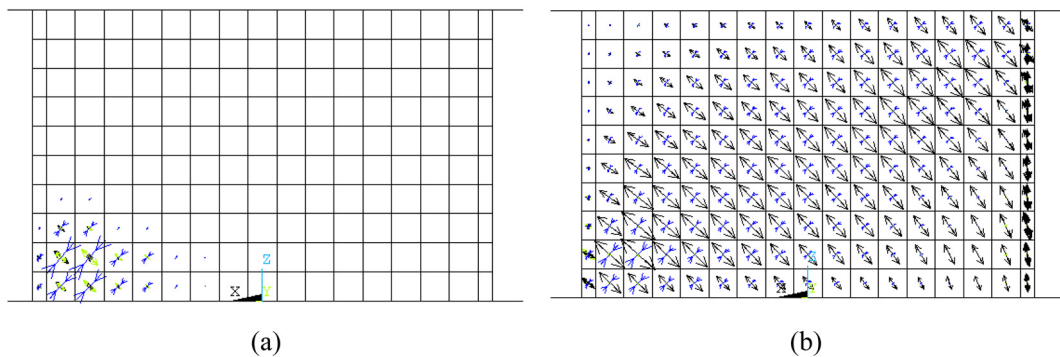(a)   (b)

Fig. 10 Vector plot displaying the direction of principal strains developed in the web at top displacement of 5.5 mm: (a) plastic strains, (b) total strains

subjected to high tensile strains in the direction normal to the compression is softer and weaker than concrete in a standard cylinder test. Vecchio and Collins (1993) introduced a softening factor as a function of principal tensile and compressive strain to decrease this peak compressive stress and strain of unconfined concrete for simplified shear design. This factor has the form

$$\beta = \frac{f_{c2max}}{f_c} = \frac{1}{0.85 - 0.27\dfrac{\varepsilon_1}{\varepsilon_3}} \le 1.0 \tag{10}$$

where f_{c2max} is the softened peak compressive strength.

Tracking the ratio of principal tensile strain to principal tensile stress ($\varepsilon_1/\varepsilon_3$) from the analysis results at the compression region, the curves in Fig. 11 showing the ($\varepsilon_1/\varepsilon_3$) ratio with respect to increasing deformation were obtained for the results of three plasticity models. Under increasing shear forces, both the principal compressive strain, ε_3, and the principal tensile strain, ε_1, increases proportionally. Prior to yield of the reinforcement, the ratio $\varepsilon_1/\varepsilon_3$ remains reasonably constant for the three cases. For the range of interest all three curve yields a ratio of approximately -2.

Compressive stress strain relationship of diagonally cracked concrete can be modified in one of two ways (ASCE-ACI committee report 1998). The loading can be assumed to be proportional, causing both the principal compressive strain, ε_3, and the principal tensile strain, ε_1, to increase simultaneously. As shown in Fig. 11, the ratio ($\varepsilon_1/\varepsilon_3$) remains reasonably constant prior to yield of reinforcement. Modifications were made to both the peak stress and the strain at peak stress. This method is suitable for static-monotonic analyses, since the initial stiffness is not affected. In the second case, it is assumed that concrete was sequentially subjected to extensive tensile strains first and then the principal compressive strain is increased. While the second case is not a realistic situation for concrete under monotonic loading, it is a better approach for concrete that has already cracked under cyclic loading. Only the stresses are modified in the second case.

Using the value of -2 for the ($\varepsilon_1/\varepsilon_3$) ratio, Eq. (10) yields a stress softening factor $\beta \approx 0.72$. The original and modified stress-strain curves of concrete are plotted in Fig. 12. The concrete peak stress has a value of $f_{c2} = 20.5$ MPa (0.72×28.6 MPa). For the bilinear case this reduces to $(f_{c2})_{ave} = 17.5$
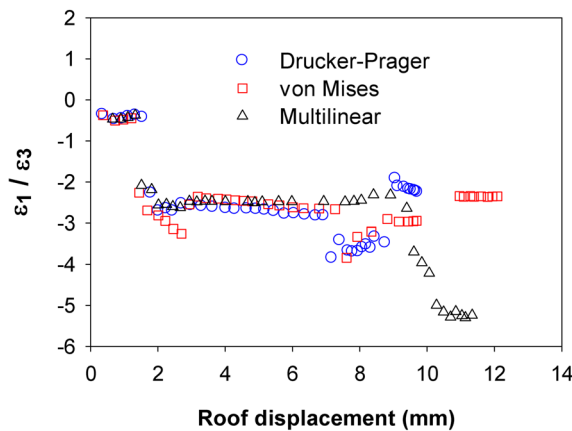

Fig. 11 The ratio of principal tensile strain to principal tensile stress ($\varepsilon_1/\varepsilon_2$) during the analysis at the compression region
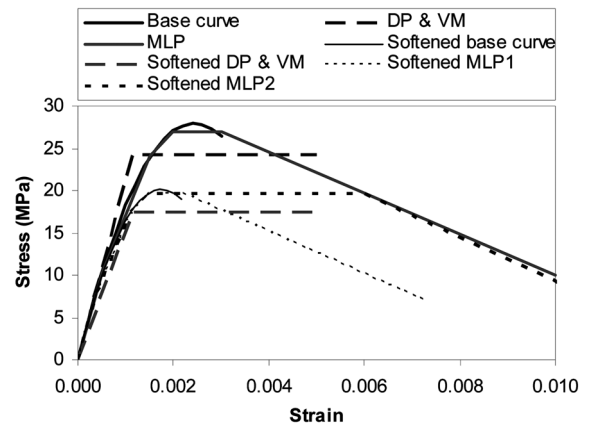
Fig. 12 Concrete stress-strain curve for original and softened states
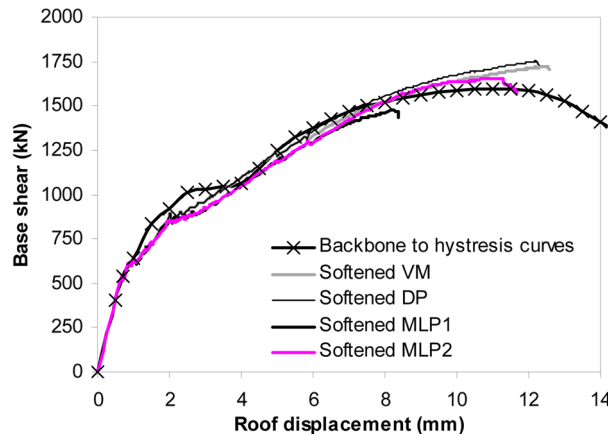
Fig. 13 Recalculated load-deflection curves plotted in comparison with the backbone curve plotted against the hysteretic curves of the five experiments

MPa by applying the factor of 0.85. However, it will be shown next that a reduction in concrete stiffness must be taken into account for accurate prediction of response in the dynamic analyses. The modulus of elasticity of the softened concrete reduces to approximately 15,000 MPa (0.72×20700 MPa).

For the von Mises and multilinear plasticity material models the softened curves given in Fig 12 are used. Assuming the concrete strength as 17.5 MPa and the stress state biaxial, the new set of material constants for the DP model can be calculated as $c = 7.144$ MPa and $\phi = 11.54^{\circ}$, respectively. The load-deflection curves calculated with softened material models are given in Fig 13. For multilinear plasticity, the softened material curve designated as MLP1 in Fig. 12 was used first. In Fig. 13 it is seen that the load-deflection curve calculated with MLP1 model experiences a premature softening. The softened multilinear curve in the yield plateau is extended to intersect with the descending branch of the original curve, which corresponds to softened multilinear curve designated as MLP2 in Fig. 12. Now the multilinear plasticity model can successfully mark the location where the strength degradation started in the experimental curve in Fig. 13.

There was a problem in calculation of the descending branch of the load-deflection curve because the solution experienced significant convergence problems. Nevertheless, considering the drift at 100 percent of ultimate load as the most appropriate definition of ultimate drift limit from engineering point of view (Duffy *et al.* 1994), the results provides considerable insight on the displacement capacity of the specimen.

5. Nonlinear dynamic time history analyses

The derivation of the most correct material parameters was discussed in detail above. It was shown that compression softening has a significant impact on accurate estimation of dynamic load-deformation envelope of the structure. Adopting the reduced bilinear curve for von Mises and Drucker-Prager plasticity with material properties of $f_c = 17.5$ and $E_c = 20,700$ MPa in Fig. 12, nonlinear time history analyses were carried out. Five table motions were applied on the model sequentially. The damping ratio for each analysis was specified with Rayleigh damping constants
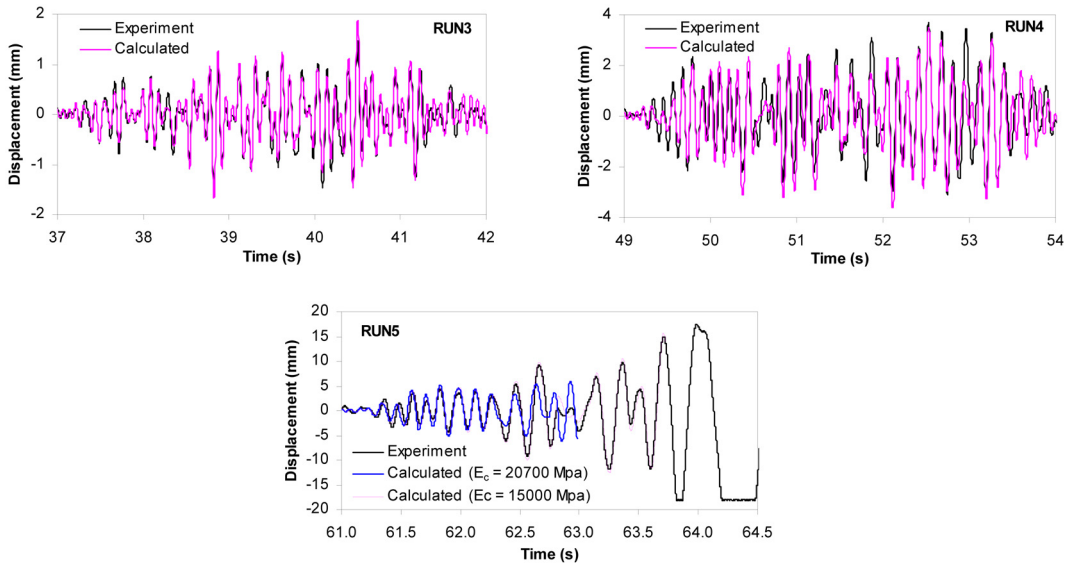
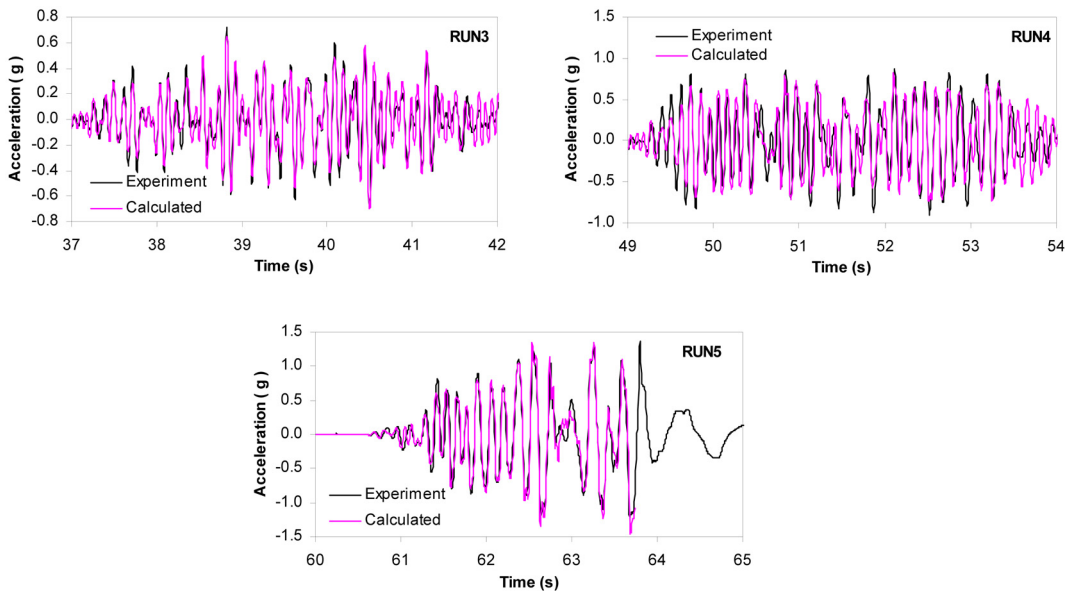Fig. 14 Displacements measured and calculated on top slab

Fig. 15 Accelerations measured and calculated on top slab

(alpha and beta) that yielded the values given in Table 2. The dynamic analyses procedure described in Kazaz *et al*. (2006) was utilized.

The computed top slab displacement and horizontal acceleration response are plotted in Fig. 14 and 15, respectively. Accelerations were converted to inertia forces. For the sake of brevity, only the nonlinear time history results obtained in RUN-5 are discussed here because the preceding tests had resulted in elastic to moderately inelastic response in the structure only, and the simulations were insensitive to material models and their parameters until the conclusion of RUN-4. In Fig. 14(c),
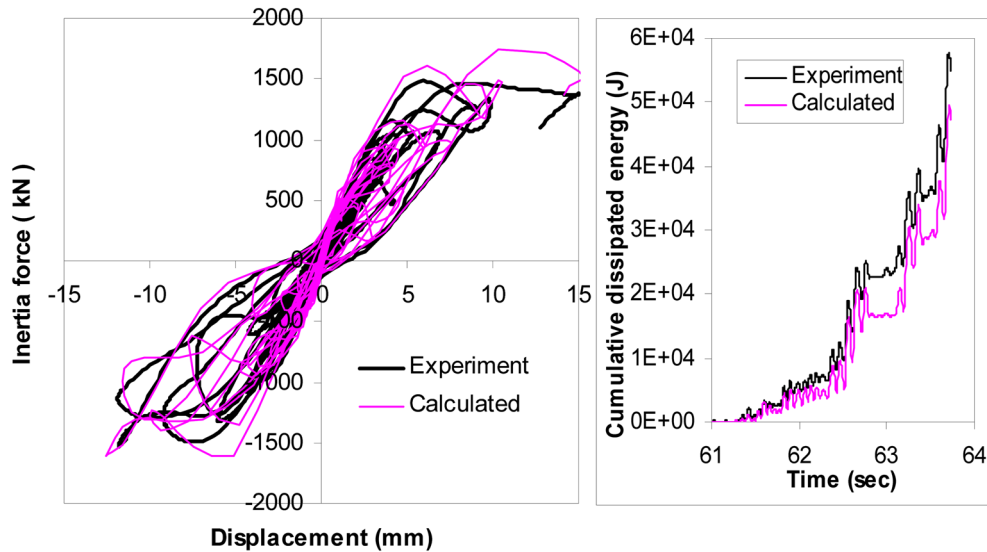
Fig. 16 Hysteresis and cumulative dissipated energy comparison plots for RUN-5

two displacement response curves are plotted for RUN-5. In the first case response was calculated by using the bilinear elasto-plastic curve with elastic modulus $E_c = 20,700$ MPa as described above. Significant disagreement is observed between the experimental and predicted response as the displacement level of 5 mm was exceeded. This must be attributed to shortcoming of the material model in accounting the effects of stiffness and strength degradation at increased inelastic displacements. In ANSYS stiffness degradation is due only to cracking of concrete. The plasticity models can not be used to model stiffness and strength degradation of concrete directly. To account for stiffness degradation, the stress-strain curve used in this last analysis must be altered to one with the same yield strength ($f_c = 17.5$ MPa) but a reduced modulus of $E_c = 15,000$ MPa. It is important to note here that cracks and plastic actions developed in the model during the previous loading history were stored as initial conditions for the finite element model. Not only significant improvement was provided but also the experimentally measured response was replicated quite well. In Fig. 16 the hysteric response calculated in RUN-5 was compared with the experiment. These yield very similar
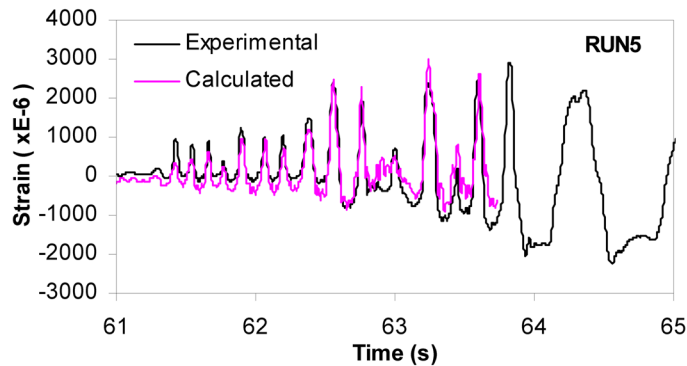

Fig. 17 Comparison of strain in the outer face of the flange-web wall intersection developed in RUN-5

Table 3 Summary of computed time history results

	Top slab horizontal response acceleration and inertial force		Top slab horizontal response displacement	Horizontal rebar strain in web wall ($\times 10^{-6}$)	Vertical rebar strain in flange wall bottom ($\times 10^{-6}$)	
	g	kN	mm		Left flange	Right flange
RUN1	0.19 (*0.21*)	231 (*253*)	0.29 (*0.29*)	20 (*9*)	146 (*45*)	143 (*-37*)
RUN2	0.38 (*0.41*)	460 (*485*)	0.55 (*0.58*)	35 (*24*)	-89 (*-92*)	-90 (*-72*)
RUN2D	0.57 (*0.62*)	683 (*739*)	1.26 (*1.05*)	437 (*126*)	-99 (*-159*)	-100 (*-125*)
RUN3	0.70 (*0.72*)	840 (*856*)	1.87 (*1.63*)	562 (*679*)	-186 (*-222*)	-77 (*144*)
RUN4	0.91 (*0.90*)	977 (*1069*)	3.61 (*3.72*)	605 (*1021*)	765 (*1036*)	924 (*893*)
RUN5[a]	1.46 (*1.37*)	1743 (*1628*)	15.72 (*15.0*)	2646 (*>5000*)	2999 (*2632*)	3123 (*2885*)

[a]Analysis stopped due to non-convergent solution.

patterns. Cumulative dissipated energy in measured and calculated hysteresis loops was also plotted in Fig. 16 to display the good matching more clearly. In Fig. 17, total strain developed at the tip of the outer face of the flange-web wall intersection during RUN-5 is plotted.

The analysis was interrupted due to non-convergence several times in RUN-5. Since the displacement level of 12 mm was surpassed when strength degradation was observed (see Fig. 13), it was decided to terminate the execution. This point was very close to when the saturation of the instrument measurements initiated in the experiment due to failure of the specimen.

In Table 3 the predicted response maximum values are tabulated. The values in parentheses are the experimental counterparts of the calculated values.

It can be concluded that by analyzing a preliminary simplified model, much insight could be gained into the behavior. Preliminary nonlinear static analyses helped in understanding the various aspects of the nonlinear dynamic response before embarking on the final nonlinear transient dynamic analysis.

6. Conclusions

In this article, a shear critical reinforced concrete shear wall specimen tested dynamically on a shaking table has been studied in order the ascertain the effectiveness of simple plasticity models for concrete in estimating the measured dynamic response of the specimen. Necessary modifications of material stress-strain response have been described and verified. The three plasticity models satisfactorily estimated the load-deformation response of the test specimen. The necessary modifications to static analyses to estimate the dynamic failure envelope were described. A pushover analysis can generate load-deflection response within a reasonable range of error, but a cyclic analysis provides a better estimation of the expected forces and displacements. Uncertainties and labor in nonlinear dynamic analyses manifest nonlinear static analyses under prescribed loads as an indispensable component of dynamic seismic response assessment.

The ratio of principal tensile strain to compressive strain in the compression region of shear wall members can be used to predict the extent of softening of concrete in compression. This is a useful procedure especially when advanced material models capable of accounting such effects automatically were not available.

Plasticity theory used within the continuum mechanics framework for the analysis of shear dominated structural elements should lead to improvements in the design and analysis of special structural systems. This study may provide guidance for the application of nonlinear finite element analyses of shear members in practical applications due to simplicity of material models and finite elements used.

Acknowledgements

References

ASCE-ACI Committee 445 on shear and Torsion (1998), "Recent approaches to shear design of structural concrete", *J. Struct. Eng. - ASCE*, **124**(12), 1375-1417.

ANSYS R9.0. (2004), Swanson Analyses System.

Bali, I. and Hwang, S.J. (2007), "Strength and deflection prediction of double-curvature reinforced concrete squat walls", *Struct. Eng. Mech.*, **27**(4), 501-521.

Belarbi, A. and Hsu, T.T.C. (1995), "Constitutive laws of softened concrete in biaxial tension compression", *ACI Struct. J.*, **92**(5), 562-573.

Červenka, J., Bažant, Z.P. and Wierer, M. (2005), "Equivalent localization element for crack band approach to mesh-sensitivity in microplane model", *Int. J. Numer. Method. Eng.*, **62**(5), 700-726.

Chen, W.F. (1982), *Plasticity in reinforced concrete*, McGraw-Hill Book Co., New York.

Drucker, D.C. and Prager, W. (1952), "Soil mechanics and plastic analysis or limit design", *Q. Appl. Math.*, **10**(2), 157-165.

Duffey, T.A., Farrar, C.R. and Goldman, A. (1994), "Low-rise shear wall ultimate drift limits", *Earthq. Spectra.*, **10**(4), 655-674.

Jirasek, M. and Bazant, Z.P. (2001), *Inelastic analysis of structures*, Wiley, Newyork.

Hemmaty, Y. (1998), "Modeling of the shear force transferred between cracks in reinforced and fiber reinforced concrete structures", *ANSYS Conference*, Pittsburg, PA.

Kazaz, I., Yakut, A. and Gülkan, P. (2006), "Numerical simulation of dynamic shear wall tests: a benchmark study", *Comput. Struct.*, **84**(8), 549-562.

Kupfer, H., Hilsdorf, H.K. and Rüsch, H. (1969), "Behavior of concrete under biaxial stress", *ACI Struct. J.*, **66**(8), 656-666.

Kwan, W.P. and Billington, S.L. (2001), "Simulation of structural concrete under cyclic load", *J. Struct. Eng. - ASCE*, **127**(12), 1391-1401.

Maekawa, K., Pimanmas, A. and Okamura, H. (2003), *Nonlinear mechanics of reinforced concrete*, Spon press, Newyork.

Mirmiran, A., Zagers, K. and Yuan, W. (2000), "Nonlinear finite element modeling of concrete confined by fiber composites", *Finite Elem. Anal. Des.*, **35**(1), 79-96.

OECD/NEA/CSNI. (1996), *Seismic shear wall ISP NUPEC's seismic ultimate dynamic response test - Comparison Report*, NEA/CSNI/R(96)10, OECD/GD(96)188.

Padmarajaiah, S.K. and Ramaswamy, A. (2002), "A finite element assessment of flexural strength of prestressed concrete beams with fiber reinforcement", *Cement Concrete Comp.*, **24**(2), 229-241.

Ramaswamy, A., Barzegar, F. and Voyiadjis, G.Z. (1994), "A post-cracking formulation for finite element analysis of RC structures based on secant stiffness", *J. Eng. Mech. - ASCE*, **120**(12), 2621-2640.

Shayanfar, M.A. and Safiey, A. (2008), "Hypoelastic modeling of reinforced concrete walls", *Comput. Concrete*,

5(3), 195-216.

Swamy, R.N. and Qureshi, S.A. (1974), "An ultimate shear strength theory for reinforced concrete T-beams without web reinforcement", *Mater. Constr.*, **7**(39), 181-189.

Thomas, J. and Ramaswamy, A (2006), "Finite element analysis of shear critical prestressed SFRC beams", *Comput. Concrete*, **3**(1), 65-77.

Vecchio, F.J. and Collins, M.P. (1986), "Modified compression-field theory for reinforced concrete elements subjected to shear", *ACI Struct. J.*, **83**(2), 219-231.

Vecchio, F.J. and Collins, M.P. (1993), "Compression response of cracked reinforced concrete", *J. Struct. Eng. - ASCE,* **119**(12), 3590-3610.

von Mises, R. (1928), "Mechanik der plastischen Formänderung von Kristallen", *Z. Angrew. Math. Mech.*, **8**(3), 161-185.

Willam, K.J. and Warnke, E.D. (1975), "Constitutive model for the triaxial behavior of concrete", *Int. Assoc. Bridge Struct. Eng. Proc.*, **19**, 174-203.

Yin, W.S., Su, E.C.M., Mansur, M.A. and Hsu, T.T.C. (1987), "Response of plain concrete to cyclic tension", *ACI Mater. J.*, **84**(5), 365-373.

CC